ACS NANO

www.acsnano.org

Electrically Tunable Nonequilibrium Optical Response of Graphene

Eva A. A. Pogna, Andrea Tomadin, Osman Balci, Giancarlo Soavi, Ioannis Paradisanos, Michele Guizzardi, Paolo Pedrinazzi, Sandro Mignuzzi, Klaas-Jan Tielrooij, Marco Polini, Andrea C. Ferrari,* and Giulio Cerullo*

Cite This: *ACS Nano* 2022, 16, 3613−3624

Read Online

ACCESS | Metrics & More | Article Recommendations

ABSTRACT: **The ability to tune the optical response of a material via electrostatic gating is crucial for optoelectronic applications, such as electro-optic modulators, saturable absorbers, optical limiters, photodetectors, and transparent electrodes. The band structure of single layer graphene (SLG), with zero-gap, linearly dispersive conduction and valence bands, enables an easy control of the Fermi energy, E_F, and of the threshold for interband optical absorption. Here, we report the tunability of the SLG nonequilibrium optical response in the near-infrared (1000−1700 nm/0.729−1.240 eV), exploring a range of E_F from −650 to 250 meV by ionic liquid gating. As E_F increases from the Dirac point to the threshold for Pauli blocking of interband absorption, we observe a slow-down of the photobleaching relaxation dynamics, which we attribute to the quenching of optical phonon emission from photoexcited charge carriers. For E_F exceeding the Pauli blocking threshold, photobleaching eventually turns into photoinduced absorption, because the hot electrons' excitation increases the SLG absorption. The ability to control both recovery time and sign of the nonequilibrium optical response by electrostatic gating makes SLG ideal for tunable saturable absorbers with controlled dynamics.**

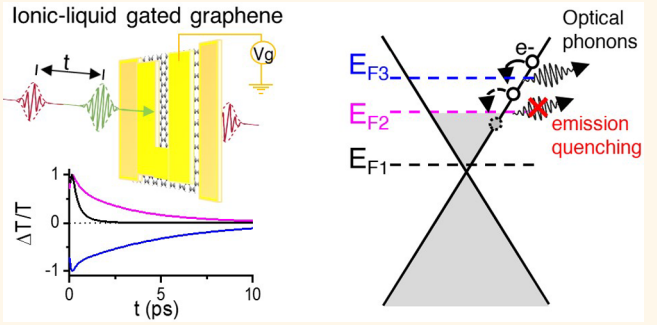

KEYWORDS: *graphene, cooling dynamics, hot electrons, tunable dynamics, optical phonons, phonon bottleneck*

INTRODUCTION

Single-layer graphene (SLG) has unique optoelectronic properties,[1−3] which stem from the physics of its massless Dirac fermions. These include high electron mobility (>100 000 $cm^2\ V^{-1}\ s^{-1}$ at room temperature (RT)[4−7]), broadband optical absorption,[8] tunability of Fermi energy, E_F, via electrostatic gating,[9] resulting from the linear dispersion of conduction (CB) and valence bands (VB), and a vanishing density of states at the Dirac point.[10]

Light absorption in SLG is due to the interplay of intraband[11−13] and interband[14,15] transitions. In undoped SLG, the first ones dominate in THz[16] and microwaves,[17] the second[14] in near-infrared (NIR)[15] and visible (VIS).[14] Electrical control of E_F, by exploiting the band-filling effect,[18] allows one to vary the density of electronic states available for both intraband[15] and interband transitions,[3,18] thus affecting the linear absorption of SLG over a broad range from THz[19−23] to NIR[24−27] and VIS.[28] This led to the development of SLG-based electro-optic modulators,[3,24,25,27,29−33] which can reach higher modulation speed (up to 200 GHz[34]) than $LiNbO_3$[35] and Si[36] because of the superior mobility of SLG charge carriers, with high modulation depths both in amplitude (up to ∼60%)[3,19,21,24,26] and phase (∼65°).[3,31]

SLG also exhibits large nonlinear optical response[37−41] because of a strong coupling to light. The third-order nonlinear optical susceptibility of SLG in the NIR at 0.7 eV is[37] $\chi^3 \sim 5 \times 10^{-18}\ m^2V^{-2}$, several orders of magnitude higher than in dielectrics (e.g., $\sim 10^{-22} m^2V^{-2}$ for SiO_2[42]) and atomically thin semiconductors (e.g., $\sim 6 \times 10^{-20}\ m^2\ V^{-2}$ for single-layer WSe_2[43]). Nonlinearities of higher order have been exploited for high-harmonics generation in SLG.[38,39] The strong nonlinear response results also in saturable absorption,[44] optical Kerr effect,[45] and optical bistability,[46,47] i.e., the ability

Received: June 10, 2021
Accepted: January 6, 2022
Published: February 21, 2022

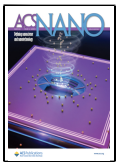

https://doi.org/10.1021/acsnano.1c04937
ACS Nano 2022, 16, 3613−3624

to provide two stable optical outputs for a specific light input.[48] E_F control via external gating allows one to tune the nonlinear optical response of SLG, resulting in gate-tunable third-harmonic generation[37,40,41] and four-wave-mixing.[49]

The E_F dependence of the transient absorption properties of SLG when brought out of equilibrium remains still largely unexplored, with studies limited to the THz range,[50−53] discussing the tuning of intraband photoconductivity with E_F.[50−52] The modulation of interband absorption in NIR and VIS is more challenging to study because E_F needs to be ∼0.5 eV in order to cross the Pauli blocking threshold, above which the nonequilibrium optical properties have been only theoretically explored.[54]

The nonequilibrium optical response of SLG is crucial for optoelectronic applications, such as photodetectors,[55] relying on the relaxation dynamics of photoexcited charge carriers. Numerous ultrafast optical spectroscopy experiments were performed on SLG[56−60] to investigate the charge-carriers relaxation dynamics by looking at the modifications it induces on SLG absorption. In a pump−probe experiment, the system is photoexcited by an optical pulse, the pump, whose duration is to be shorter than the time scale of the relaxation processes under investigation. The relaxation of the photoexcited system is then monitored by detecting the absorption of a second optical pulse, the probe, as a function of the time delay with respect to the pump pulse.[61]

In SLG, interband absorption of the pump pulse induces out-of-equilibrium distributions of holes (h) and electrons (e) in VB and CB, respectively, peaked at $\pm \hbar\omega_{pump}/2$, where $\hbar\omega_{pump}$ is the pump photon energy. Carrier-carrier scattering drives the ultrafast e−h thermalization on a time-scale $\tau_{th} < 20$ fs[60] from out of equilibrium, to hot Fermi−Dirac distributions (HFD) with defined electronic temperature, T_e. The HFD can be detected in a pump−probe experiment as a photobleaching (PB) signal,[56−58] i.e., decreased probe absorption compared with equilibrium, because of Pauli blocking of interband transitions caused by the photogenerated e/h. The excess energy of the hot charge-carriers is released to the lattice via electron−phonon scattering with optical phonons,[62−64] anharmonically coupled to acoustic phonons.[62−65] Hot carriers' cooling occurs on a few-ps time-scale[56−58,60,65] and is influenced, through the activation of additional relaxation channels, by the dielectric environment (e.g., via near-field coupling to hyperbolic optical phonons of substrate or encapsulant material[66]). Defects can also accelerate the cooling via electron−phonon interaction, by acting as scattering centers mediating the direct coupling of the hot charge carriers with finite momentum acoustic phonons.[67−69] This process, referred to as supercollision,[67−69] accelerates the cooling for increasing defect density.[70]

Here we investigate the E_F dependence of the nonequilibrium optical response of SLG in the NIR range between 0.729 and 1.240 eV (1000−1700 nm), exploiting ionic liquid gating to tune E_F from −650 to 250 meV, thus exceeding the Pauli blocking threshold for interband absorption, achieved when $|E_F| = \hbar\omega_{probe}/2$, where $\hbar\omega_{probe}$ is the energy of the probe beam. Applying ultrafast pump−probe spectroscopy with 100 fs time resolution, we detect the changes with E_F of amplitude and sign of the differential transmission ($\Delta T/T$), as well as of its relaxation dynamics. Starting from not intentionally doped SLG and increasing E_F, we first observe a rise in PB amplitude ($\Delta T/T > 0$) with a slow-down of its relaxation dynamics. Above the Pauli blocking threshold, photoexcitation has an opposite effect on SLG, activating additional absorption channels, as shown by the appearance of photoinduced absorption (PA) ($\Delta T/T < 0$). The $\Delta T/T$ changes are assigned to the E_F dependence of the hot carriers cooling dynamics, simulated considering relaxation through emission of optical phonons. The gate tunability of the nonequilibrium optical response is key for optoelectronic applications, such as saturable absorbers (SA) with gate-tunable response.

RESULTS AND DISCUSSION

We modulate E_F by means of the electrostatic field effect[71] using an ionic-liquid top-gated field effect transistor (FET) sketched in Figure 1a. The top-gate geometry, with

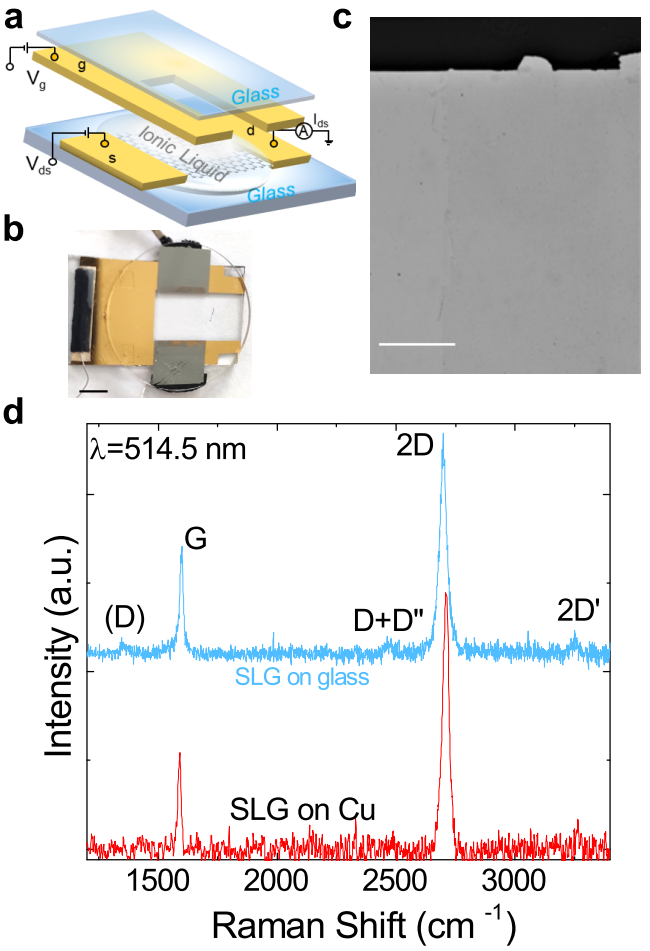

Figure 1. (a) Schematic of device with source (s), drain (d) and gate (g) contacts used to tune the SLG E_F while measuring its transmission properties. (b) Photo of representative device. Scale bar 5 mm. (c) Image of transferred SLG in a region near the drain contact (dark area on the top). Scale bar: 100 μm. (d) 514.5 nm Raman spectrum of SLG as-grown and transferred on glass.

diethylmethyl (2-methoxyethyl) ammoniumbis(trifluoromethylsulfonyl)imide ($C_6H_{20}F_6N_2O_5S_2$) as ionic liquid, is chosen to allow light measurements in transmission through a ∼1 cm^2 optical window. Large area (8 mm × 8 mm) SLG is prepared by chemical vapor deposition (CVD) as for ref 72. The device fabrication follows ref 73. Figure 1b is a photo of

https://doi.org/10.1021/acsnano.1c04937
ACS Nano 2022, 16, 3613−3624

the device, and Figure 1c an optical image of the transferred SLG, showing no macroscopic tearing nor folding.

Both as-grown and transferred SLG are characterized with a Renishaw InVia Raman spectrometer using a 50× objective, a CW laser at 514.5 nm, with power on the sample <0.5 mW to exclude heating effects. The Raman peaks are fitted with Lorentzians, with error bars derived from the standard deviation across 6 measurements and the spectrometer resolution ∼1 cm^{-1}. The Raman spectrum of as-grown SLG on Cu is in Figure 1d, after Cu photoluminescence removal.[74] The 2D peak is a single Lorentzian with full-width half-maximum FWHM(2D) ∼31 ± 3 cm^{-1}, a signature of SLG.[75] The G peak position Pos(G) is ∼1586 ± 2 cm^{-1}, with FWHM(G) ∼ 16 ± 3 cm^{-1}. The 2D peak position, Pos(2D), is ∼2704 ± 4 cm^{-1}, while the 2D to G peak intensity and area ratios, $I(2D)/I(G)$ and $A(2D)/A(G)$, are 3.1 ± 0.4 and 6.2 ± 0.7. No D peak is observed, indicating negligible Raman active defects.[76,77]

The Raman spectrum of SLG transferred on glass is in Figure 1d. The 2D peak retains its single-Lorentzian line shape with FWHM(2D) ∼ 36 ± 1 cm^{-1}. Pos(G) ∼ 1597 ± 1 cm^{-1}, FWHM(G) ∼ 15 ± 1 cm^{-1}, Pos(2D) ∼ 2696 ± 1 cm^{-1}, $I(2D)/I(G)$ ∼ 2 ± 0.2 and $A(2D)/A(G)$ ∼ 4.9 ± 0.3, indicating p-doping with E_F ∼ −230 ± 80 meV.[71,78] $I(D)/I(G)$ ∼ 0.06 ± 0.05 corresponds[79] to a defect density ∼2.6 ± 1.9 × 10^{10} cm^{-2} for excitation energy 2.41 eV and E_F = −230 ± 80 meV. Pos(G) and Pos(2D) are affected by the presence of strain.[80] For uniaxial(biaxial) strain, Pos(G) shifts by $\Delta Pos(G)/\Delta\varepsilon$ ∼ 23(60)cm^{-1}%$^{-1}$.[80,81] Pos(G) also depends on E_F.[9,71] The average doping as derived from $A(2D)/A(G)$, FWHM(G) and $I(2D)/I(G)$, should correspond to Pos(G) ∼ 1588 ± 1 cm^{-1} for unstrained graphene.[9,71] However, we have Pos(G) ∼ 1597 ± 1 cm^{-1}, which implies a contribution from uniaxial (biaxial) strain ∼0.16 ± 0.02% (0.4 ± 0.04%).[80,81]

The gate voltage, V_g, polarizes the ionic liquid leading to the formation of electrical double layers (EDLs), near SLG and Au interfaces,[71,82] that modulate the carrier density. Since the EDL thickness is ∼1 nm for ionic liquids,[83,84] the solid−liquid interfacial electric field and the induced charge densities on the surface reach values as large as[22,83] ∼10−20 MV cm^{-1} and 10^{14} cm^{-2} even at moderate V_g ∼ 1−2 V. The transfer characteristics of our device for source-drain bias V_{ds} = 100 mV is in Figure 2a. This exhibits a typical ambipolar behavior, as seen by the V-shaped gate dependence of the source-drain current I_{ds}. The channel resistance peaks at V_{CNP} = 0.84 V, corresponding to the charge neutrality point (CNP), where the density of states in SLG reaches its minimum.[22,23,85] V_{CNP} depends on E_F, on the gate-metal work function,[22] and on the choice of contact materials.[86]

In order to determine E_F as a function of V_g, we measure the static transmission T in NIR (500−1500 meV) with an Agilent Cary 7000 spectrometer. Figure 2b plots a selection of transmission spectra for different V_g, compared with that at the CNP, evaluated as $\delta T/T = \frac{T(V_g) - T(V_{CNP})}{T(V_{CNP})}$. T increases with respect to the CNP, i.e., $\delta T/T > 0$, when absorption is inhibited by Pauli blocking, due to e in CB (n-doping) or h in VB (p-doping). In terms of probe photon energy, this corresponds to $\hbar\omega_{probe} < 2|E_F|$. We estimate E_F considering that $\delta T/T$ halves[73] for $\hbar\omega_{probe} = 2|E_F|$ at values indicated by black stars in Figure 2b. For probe photon energies $\hbar\omega_{probe} < 2|E_F|$, interband absorption is blocked, and the sample has T ∼ 99.6−99.8%, with ∼0.2−0.4% residual absorption being attributed to intraband transitions enabled by disorder.[73] The T modulation due to the bleaching of interband absorption is ∼1.5% against the ∼2.3% expected for suspended SLG,[8] because of the presence of the glass substrate and of diethylmethyl (2-methoxyethyl) ammoniumbis(trifluoromethylsulfonyl)imide,[87] with a refractive index ∼1.418−1.420.[88]

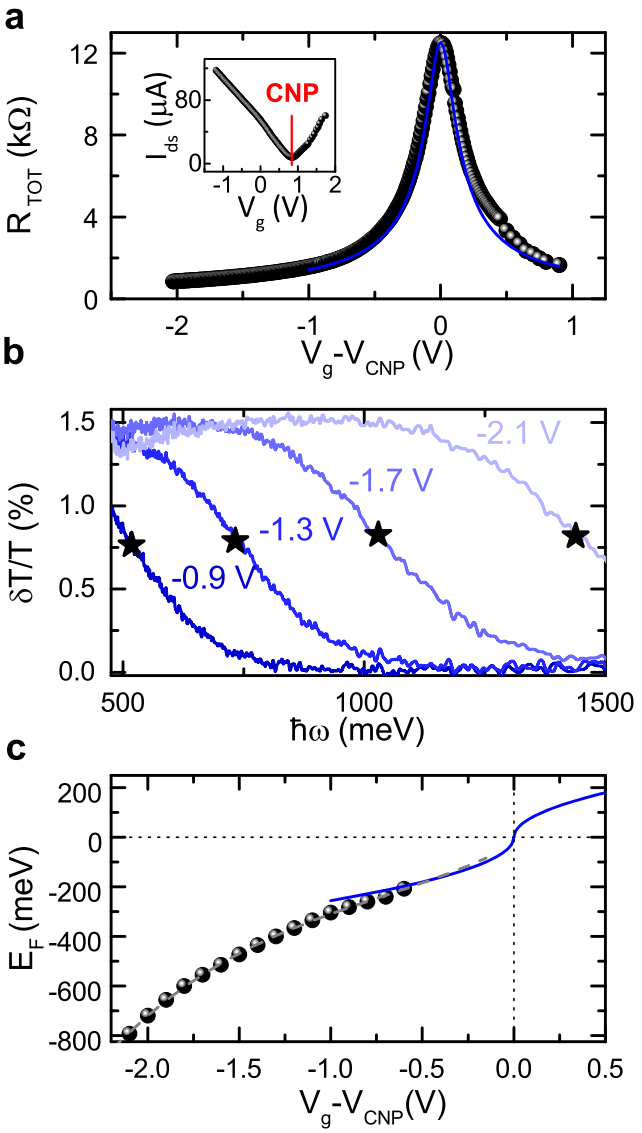

Figure 2. (a) Total resistance R_{TOT} as a function of V_g-V_{CNP} (black dots) with Drude model fitting (blue solid line) to estimate residual charge carrier density, n_0, and gate capacitance C. Inset, I_{ds} for V_{ds} = 100 mV. (b) $\delta T/T$ for different V_g−V_{CNP} (indicated next to the curves) as a function of photon energy $\hbar\omega$, showing the gate tunability of the absorption edge for interband transitions; (c) E_F determined from $\delta T/T$ as a function of V_g−V_{CNP} (full dots) interpolated by $f(x) = A_0 + A_1x + A_2x^2 + A_3x^3$ with A_0 = −0.03 eV, A_1 = 0.37 eV/V A_2 = 0.17 eV/V^2 A_3 = 0.08 eV/V^3 (gray dashed line), together with the trend (blue solid line) $E_F = \hbar v_F\sqrt{\pi n_e(V_g)}$ where $n_e(V_g) = (V_g - V_{CNP})(C/e)$ is the gate-tunable charge carrier density

E_F extracted from the T measurements is plotted in Figure 2c as a function of V_g. At V_g = 0 V, there is a p-doping E_F ∼ −250 meV in agreement with the Raman estimation (∼−230

https://doi.org/10.1021/acsnano.1c04937
ACS Nano 2022, 16, 3613−3624

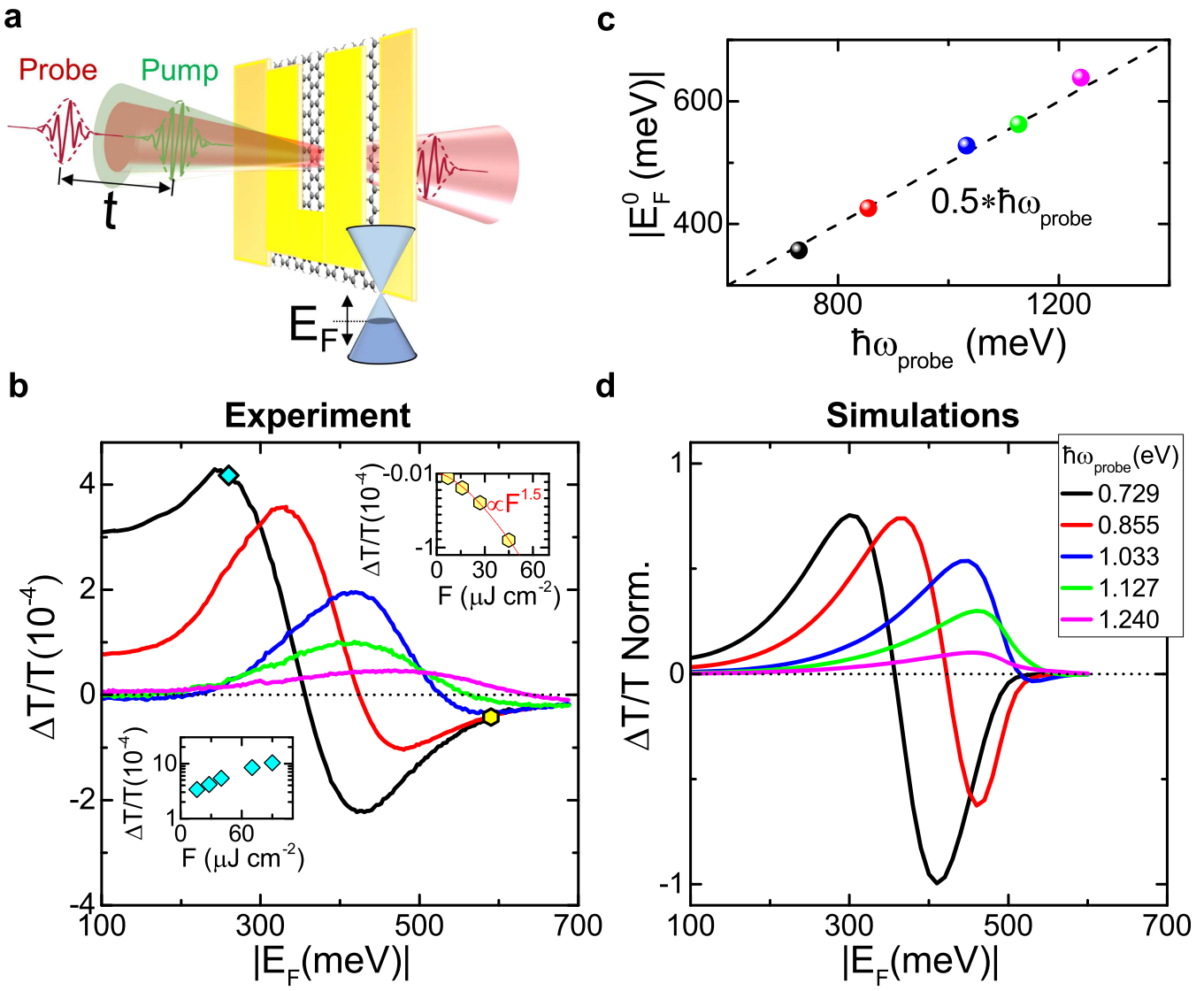

Figure 3. (a) Sketch of pump−probe experiment on SLG with tunable E_F controlled by V_g. (b) Experimental $\Delta T/T$ at t = 150 fs as a function of $|E_F|$ for p-doping acquired at different $\hbar\omega_{probe}$ = 0.729, 0.855, 1.033, 1.127, 1.240 eV (legend of panel d) for a pump fluence $F \sim 28$ μJ cm^{-2}. Top-right inset: fluence dependence of $\Delta T/T$ amplitude above Pauli blocking for pump absorption, at $\hbar\omega_{probe}$ = 0.729 eV and E_F = −590 meV (hexagonal yellow symbol in main figure), together with a superlinear power-law dependence on F (solid red line). Bottom-left inset: fluence dependence of $\Delta T/T$ amplitude, for $\hbar\omega_{probe}$ = 0.729 eV and E_F = −260 meV (cyan rhombus symbol in main figure). (c) $|E_F^0|$ at $\Delta T/T$ = 0, extracted from panel b, as a function of $\hbar\omega_{probe}$. (d) Simulated $\Delta T/T$ at t = 150 fs as a function of $|E_F|$ for p-doping at the same $\hbar\omega_{probe}$ as in panel b.

± 80 meV) without ionic liquid. From the analysis of the charge-transfer curve with the Drude model as in ref 23 (see blue line in Figure 2a), we evaluate a residual n_0 = 5.6 × 10^{11}cm^{-2}, responsible for the finite conductivity at the CNP, and a gate capacitance C = 766 nF cm^{-2}. We note this is a typical n_0 for as-grown and transferred SLG.[89] A lower residual doping ∼10^{11} cm^{-2} can be achieved with cleaning techniques,[6] not used here. The finite electrical conductivity and doping at the CNP[22,23] are due to electron−hole puddles,[90] caused by charged impurities[91] located either in the dielectric, or at the SLG/dielectric interface.[91] Near the CNP, for $|V_g - V_{CNP}| < 0.6$ V, the interband absorption edge is outside the spectral window of our $\delta T/T$ measurements, and we evaluate[8] $E_F = \hbar v_F \sqrt{\pi n_e(V_g)}$, with v_F the Fermi velocity, directly from the gate tunable charge carrier density $n_e(V_g) = (V_g - V_{CNP})(C/e)$, with e the electron charge, see blue solid line in Figure 2c. At high gate voltages $|V_g - V_{CNP}| > 0.9$ V, the disagreement between calculated E_F and the values obtained from $\delta T/T$ is attributed to the dependence of mobility on charge carrier density,[6] not included in the analysis of the transport properties used for the calculated E_F, that is valid near the CNP and fails to describe the sample behavior for $|V_g - V_{CNP}| > 0.9$ V. Accordingly, we assume the values extracted from $\delta T/T$ (Figure 2c gray dashed line) in the range $|V_g - V_{CNP}| > 0.6$ V, and those calculated from $n_e(V_g)$ (Figure 2c, blue solid line), in the range $|V_g - V_{CNP}| < 0.6$ V. At each V_g of Figure 2. We also monitor the source-drain current I_{ds} (inset of Figure 2a) to determine the empirical relation with E_F. The transfer curve that we obtain allows us to track E_F by monitoring I_{ds} during all subsequent measurements. We test the E_F tunability of the ionic liquid top-gate device up to −800 meV, corresponding to a wide range of charge carrier densities from ∼4.5 × 10^{12} cm^{-2} (n-doping) to ∼−4.7 × 10^{13} cm^{-2} (p-

https://doi.org/10.1021/acsnano.1c04937
ACS Nano 2022, 16, 3613−3624

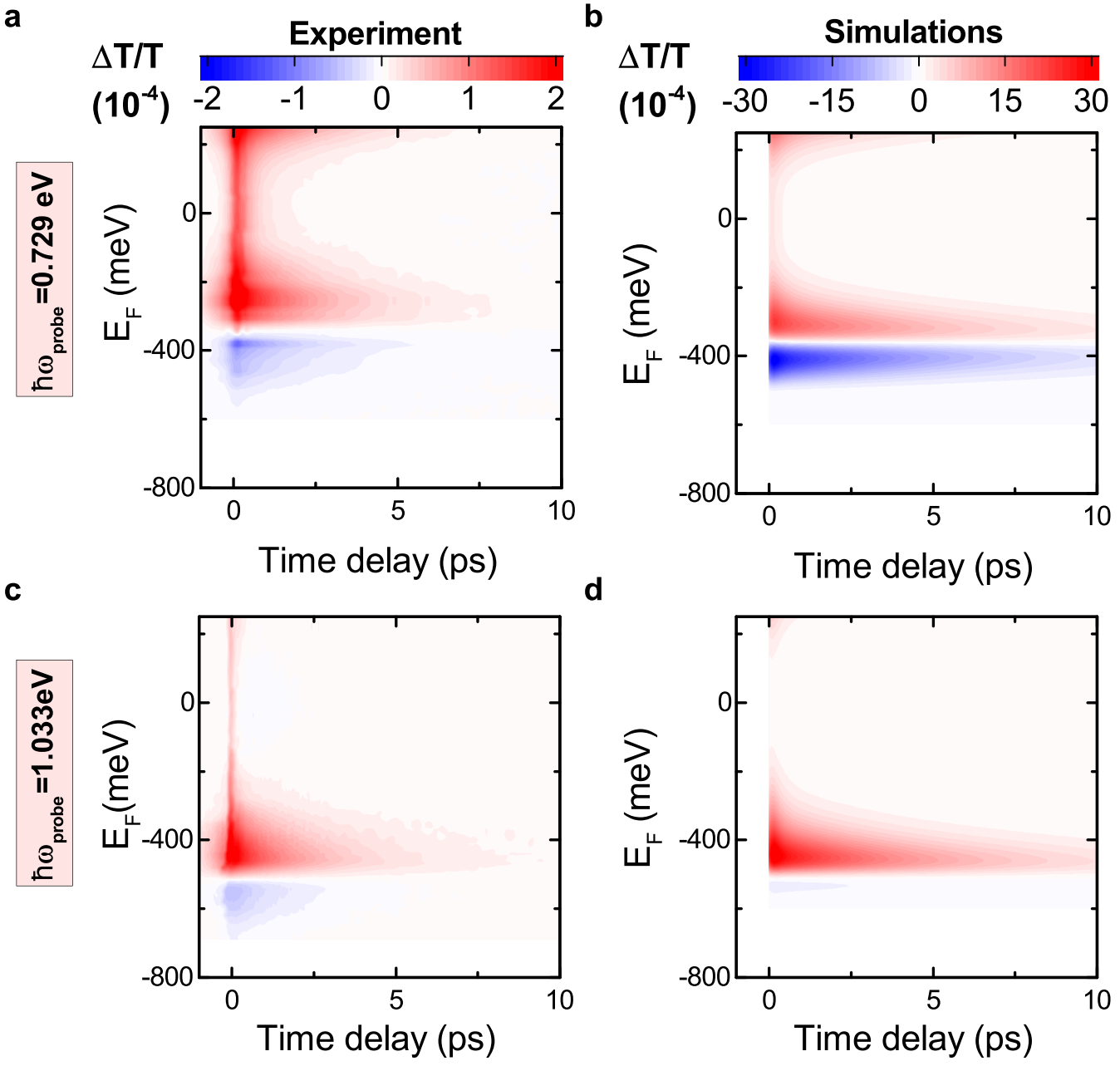

Figure 4. Time-evolution of $\Delta T/T(t)$ for different E_F at (a,b) $\hbar\omega_{probe}$ = 0.729 eV, with (a) experiment, and (b) simulations, and (c,d) $\hbar\omega_{probe}$ = 1.033 eV, with (c) experiment and (d) simulations. t = 0 corresponds to the pump arrival. The signal at negative delays indicates a finite build-up time, exceeding the pump−probe time duration at $|E_F|$ = 250 meV for $\hbar\omega_{probe}$ = 0.729 eV and 350 meV for $\hbar\omega_{probe}$ = 1.033 eV, approaching the Pauli blocking E_F.

doping), much wider than possible with a 285 nm SiO_2 back gate, usually limited to $\pm 6 \times 10^{12}$cm^{-2} by the gate capacitance.[85] We got similar $E_F(V_g)$ in ref 73 from Raman spectra and NIR transmission.

We perform ultrafast pump−probe spectroscopy as sketched in Figure 3a. The pump is a 100 fs NIR pulse centered at $\hbar\omega_{pump}$ = 0.8 eV, while the probe spectrum covers $\hbar\omega_{probe}$ = 0.729−1.240 eV (see Methods for details). The relaxation dynamics is monitored through the differential transmission $\Delta T(t)/T = \frac{T_{pump\text{-}ON}(t) - T_{pump\text{-}OFF}}{T_{pump\text{-}OFF}}$ evaluated from the probe transmission with $(T_{pump-ON})$ and without $(T_{pump-OFF})$ pump excitation, after a time delay t between probe and pump pulses, varied with an optical delay line. Given that the pulses duration exceeds the time-scale of carrier−carrier thermalization,[60] we can assume charge carriers thermalized to HFDs and investigate their cooling dynamics.

Figure 3b plots $\Delta T/T$ at t = 150 fs, chosen as the delay at which the maximum signal amplitude is reached for V_g = 0 V. The signal is plotted as a function of E_F for different probe photon energies. Since the transient response is symmetric with respect to the CNP for n- and p- doping and our SLG is p-doped at V_g = 0, we explore negative E_F in order to reach higher $|E_F|$ by applying a smaller V_g. We observe a strong modulation of $\Delta T/T$ with E_F, higher at the low-energy tail of the probe pulse, with the signal changing from 4 to -2×10^{-4}

https://doi.org/10.1021/acsnano.1c04937
ACS Nano 2022, 16, 3613−3624

(see the curve at 0.729 eV in Figure 3b). The signal amplitude decreases for increasing $\hbar\omega_{probe}$, as expected for a thermal distribution of carriers.[58] In all the probed range, near the CNP, we observe, as expected, a PB signal, i.e., $\Delta T/T(t) > 0$. By increasing $|E_F|$, first PB increases in amplitude, and then a change of sign occurs at a threshold $|E_F|$ dependent on the probe photon energy. The Fermi energy at which the sign change occurs, $|E_F^0|$ in Figure 3c, corresponds to $\hbar\omega_{probe}/2$, i.e., the Pauli blocking threshold for probe photons. Above this, the pump pulse, exciting e (h) to higher (lower) energy states, partially unblocks the probe interband absorption, otherwise inhibited, resulting in a PA signal, i.e., $\Delta T/T < 0$. The PA intensity increases with E_F up to a peak, whose position in terms of E_F raises with probe photon energy. A constant $\Delta T/T \sim -1 \times 10^{-5}$ is then approached in the high $|E_F|$ limit ($E_F < -690$ meV) in all the probed range.

We note that ref 93 reported a study of E_F dependence of the transient optical properties of SLG, without reaching Pauli blocking, i.e., $|E_F| > \hbar\omega_{probe}/2$, which we investigate here, revealing the PA regime. Our results show that, by varying V_g, we can not only control the relaxation dynamics of SLG, but also change the $\Delta T/T$ sign.

Above the Pauli blocking threshold for pump interband transitions ($|E_F| \geq 400$ meV for $\hbar\omega_{pump} = 800$ meV), $\Delta T/T$ is expected to vanish, because the pump should not be able to photoexcite SLG. However, a finite value is observed, caused by residual pump absorption, related to both extrinsic[14,73,92] and intrinsic[14,94] effects. Among the former, charged impurities and scatterers (e.g., edge defects, cracks, vacancies) can induce residual conductivity[73,92] activating intraband absorption. Amongst the latter is the residual absorption from the tail of the carrier Fermi distribution, i.e., off-resonance absorption, which has a finite broadening at RT.[94] The fluence dependence of $\Delta T/T$ at $\hbar\omega_{probe} = 0.729$ eV in the inset of Figure 3b is superlinear above the threshold for Pauli blocking of pump absorption (as measured at $|E_F| = 590$ meV), suggesting a non-negligible contribution from two-photon absorption.[95] This could also explain the vanishing signal when approaching $|E_F| = 800$ meV (the Pauli blocking threshold for two-photon absorption).

While height and width of PB and PA bands slightly change with $\hbar\omega_{probe}$, we observe similar features in all the probed range upon increasing $|E_F|$: an increase of PB, followed by a decrease, and a sign change above the Pauli blocking threshold for probe absorption. The measurements are performed using a low excitation fluence (28 μJ cm^{-2}) to work in a perturbative regime corresponding to $T_e < 1000$K, thus reducing the impact of the hot-phonon bottleneck and focusing on the electron-optical phonon cooling. The amplitude of $\Delta T/T$ increases by increasing the excitation fluence, as for the inset of Figure 3b, by almost 2 orders of magnitude for the PA signal (see top-right inset of Figure 3b at $|E_F| = 590$ meV) and 1 order of magnitude for the PB signal (see bottom-left inset of Figure 3b at $|E_F| = 260$ meV). We previously reported the use of ungated SLG as SA (GSA) in mode-locked lasers, in which an absorption modulation $\lesssim$1.3% is sufficient to induce and control the pulsed (mode-locked) regime.[44] The ability to electrically control amplitude, sign, and recovery time of $\Delta T/T$ in a GSA is thus of practical relevance for optimizing mode-locking for stability, pulse width, and average output power.

To understand the E_F dependence of the nonequilibrium optical response of SLG, we calculate $\Delta T/T$ (see Methods for details) as a function of initial carrier density n_e, related[8] to E_F by $n_e = \frac{1}{\pi}\left(\frac{E_F}{\hbar v_F}\right)^2$. $\Delta T/T$ in Figure 3d is computed from the changes in optical conductivity, $\Delta\sigma$, induced by photo-excitation as a function of E_F. To evaluate $\Delta T/T$ at $t = 150$ fs we consider the charge carriers as distributed in energy and momentum along a HFD with a time-dependent chemical potential, μ_c, and $T_e(t) >$ RT. Our model takes into account that, even though the pump fluence is constant, the initial T_e changes with E_F due to the change of pump absorption. We consider the absorption from the tail of the Fermi–Dirac distribution as source of residual pump absorption for $|E_F| >$ 400 meV. The charge carrier distribution modification with E_F is sufficient to reproduce qualitatively the experimental PB signal increase, the change of sign at $\hbar\omega_{probe}/2$, and the PA decrease for $E_F > 400$ meV, Figure 3d.

Our data and model indicate that the PA signal amplitude is maximized at $E_F \sim 0.4\hbar\omega_{probe}$, unlike claimed in ref 93, i.e., that the maximum occurs at $E_F = 0.5\hbar\omega_{pump}$. We attribute this difference to the coarser sampling of E_F in ref 93 (50 meV steps against our 4 meV, Figure 3b), to the fact that ref 93 used a reflection geometry, mixing contributions from transient reflection and transmission with opposite sign,[96] and to the larger probe photon energy at which intraband transitions contribute with opposite sign to that of interband transitions.[97] Furthermore, the E_F thresholds that control the $\Delta T/T$ amplitude and sign are identified by $\hbar\omega_{probe}$, not by $\hbar\omega_{pump}$ as incorrectly stated in ref 93, since $\hbar\omega_{pump}$ has no role in defining the cooling dynamics of the HFD after the first ultrafast (<100 fs) step of electron–electron thermalization.[60,63]

To examine the dependence of the cooling dynamics on E_F, we monitor $\Delta T/T$ as a function of pump–probe delay. Figures 4a,c show the gate-dependent relaxation dynamics at $\hbar\omega_{probe} = 0.729$, 1.033 eV, lower and higher than the pump photon energy. At both energies, the relaxation dynamics progressively slows down with increasing $|E_F|$, evolving from a biexponential to a monoexponential decay, due to a reduction of the fast decay component. We can appreciate this slowdown by noting that, to see a signal reduction by a factor 10, we need to wait ~1 ps at $|E_F| = 100$ meV and ~5 ps at 300 meV. Both signal intensity and relaxation dynamics are symmetric for *n*- or *p*-doping, as a consequence of the CB, VB symmetry.

The observed gate-dependence can be qualitatively explained considering that, for increasing $|E_F|$, the excess energy of the photoexcited charge carriers with respect to equilibrium is reduced, affecting the scattering with optical phonons that drives the cooling. To gain a deeper insight into the phenomena responsible for quenching the fast relaxation component, we solve a set of phenomenological equations of motion (EOMs)[98] for T_e and for the occupation of the phonon modes. We include the optical phonon modes at the K and Γ points of the SLG Brillouin zone, and we consider that they can be emitted/absorbed by e and h and decay into acoustic modes due to anharmonic coupling[62,63,65] (see Methods).

We calculate the time-evolution of the differential conductivity for several values of μ_c, corresponding to E_F, (i.e., μ_c at $T_e = 0$[94]), in the range 250 to −650 meV. The results in Figure 4b,d explain the observed slowdown of the dynamics with increasing E_F, with the saturation of the phase space for optical phonon-emitting electronic transitions. As E_F increases, there are fewer carriers with an energy high enough (>160 meV) to emit an optical phonon, and optical phonon emission is quenched. This is a fundamental process, not dependent on

https://doi.org/10.1021/acsnano.1c04937
ACS Nano 2022, 16, 3613–3624

the SLG substrate, like supercollision cooling through defects,[99] nor on its dielectric environment, like the cooling to hyperbolic phonons in hBN-encapsulated SLG.[66] It is determined by the intrinsic coupling of e with the K and Γ phonons.[100] The initial increase of PB amplitude with E_F in Figure 3b,c is a consequence of the quenching of relaxation via optical phonons,[60,63] which reduces the initial fast decay.

Figure 4 also shows that $|E_F^0|$ is independent of t, both in experiments and simulations. The vanishing $\Delta T/T$ does not correspond to zero absorption, but it means that the conductivity remains at its equilibrium value for all delays. For $t > 0$, the e system is photoexcited. This can happen only because the e distribution undergoes a time-evolution such that the conductivity remains time-independent at $\hbar\omega = 2|E_F|$.

Figure 5a shows that for $E_F > 340$ meV and $\hbar\omega_{probe} = 0.729$ eV, the simulations predict a further slowdown of the relaxation dynamics, not observed in our experiments. These all saturate to a similar decay trend independent of E_F (see overlapping black and green dots in Figure 5). Analogous behavior is found at all $\hbar\omega_{probe}$, provided that when we increase $\hbar\omega_{probe}$, we tune E_F to higher levels to find overlapping decay dynamics (see Figure 5b). To understand the saturation of this slowdown, we need to consider that additional relaxation channels may start playing a role once the cooling via optical phonons gets slower. Defects can accelerate cooling,[67−70] mediating the scattering with acoustic phonons of finite momentum and energy.[69] This supercollision mechanism[67−70] may become the dominating process once optical phonon emission is quenched. Cooling times ∼4 ps are expected for supercollision cooling[67] in SLG with $E_F \sim 400$ meV and mobility of a few thousand cm^2 V^{-1} s^{-1}, as that of our device. The E_F independence of the decay dynamics in the high E_F limit could be explained by the lack of dependence on carrier density of the supercollision cooling time away from the Dirac point.[67] According to refs 78 and 79, the e scattering time with defects in SLG is not expected to significantly change with E_F.

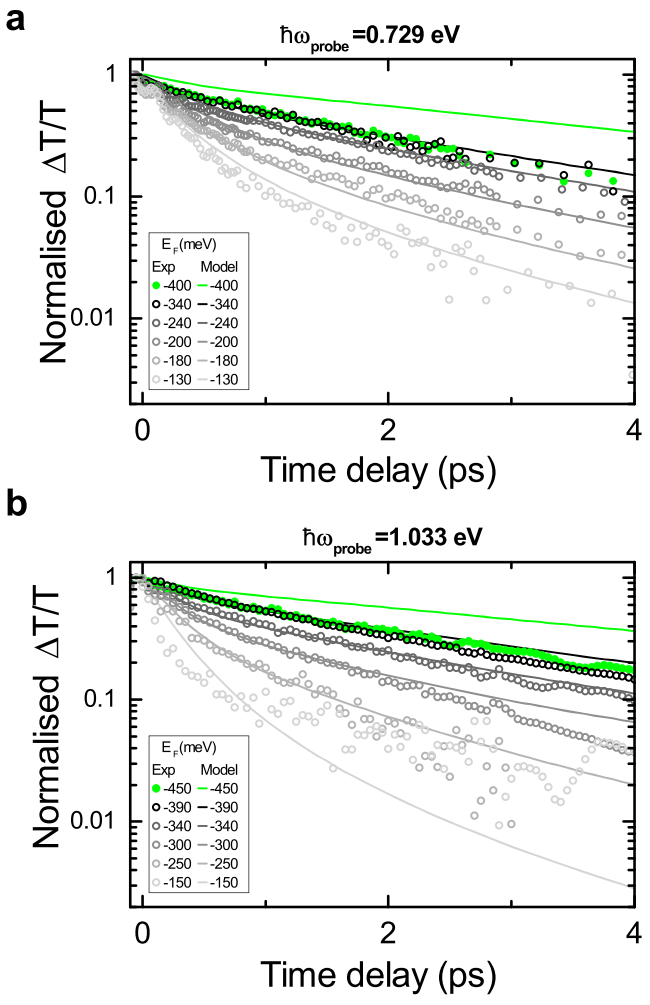

Figure 5. (a,b) Experimental (colored dots) and theoretical (solid lines) $\Delta T/T$ at different E_F for (a) $\hbar\omega_{probe} = 0.729$ eV and (b) $\hbar\omega_{probe} = 1.033$ eV for pump−probe time delays between −500 fs and 5 ps (pump arrival at $t = 0$).

The electrical tunability of the SLG relaxation dynamics, sketched in Figure 6a−c, is promising for the realization of tunable SA. Saturable absorption, i.e., the quenching of optical absorbance under intense illumination,[101] can occur in SLG at low light intensity (e.g., ∼ 0.750MW cm^{-2} at 0.8 eV[102]). We measured a saturation intensity[44] $I_S = 0.5−1.7$MW cm^{-2} for photon energies in the range ∼0.5−2.5 eV, comparable to semiconductor saturable absorber mirrors (SESAMs) ($P = 0.01−0.1$MW cm^{-2} at 0.944 eV[103]), but maintained over a much broader spectral range.[44] The modulation depth, defined as the maximum change in absorption,[101] can be optically tuned exploiting cross absorption modulation.[104] GSAs are promising for passive mode-locking,[44,105,106] Q-switching,[107] and Q-switched mode-locking.[108]

Figure 6 shows that the SLG equilibrium photoresponse can be electrically tuned, providing an additional knob for controlling its SA performance in terms of modulation depth and recovery dynamics. For $E_F \ll \hbar\omega_{probe}/2$, the intrinsic biexponential-like relaxation dynamics makes SLG an ideal fast SA, Figure 6a. The presence of two different time scales, in analogy with SESAMs,[109] is considered an advantage for mode locking.[109] As discussed in refs 109 and 110, the longer time scale reduces the saturation intensity, facilitating self-starting mode-locking, while the fast relaxation component is efficient in shaping subps pulses. For $E_F \leq \hbar\omega_{probe}/2$ as in Figure 6b, SLG can act as slow SA[111] with recovery times 10 to 30 times longer than the pulse duration,[111,112] favoring soliton shaping,[112] or the temporal shift of the pulses caused by the SA,[109] which limits the time in which noise behind the pulse can be amplified.[111] Longer recovery time also gives an increased tolerance towards instability induced by self-phase modulation.[111]

The PA at $E_F > \hbar\omega_{probe}/2$ can be exploited to operate SLG as reverse SA,[113] for which absorption increases with increasing impinging intensity, because of depletion of the final state population (see Figure 6c). The PA of highly doped SLG could be exploited to realize an optical limiter,[114] based on the decrease in transmittance under high-intensity or fluence illumination. An ideal optical limiter, with the functionality of protecting delicate optical elements, should strongly attenuate intense, potentially dangerous, laser beams, while exhibiting high transmittance for low-intensity light. Carbon nanotubes[115] and few-layer graphene[116] dispersions in organic solvents have been used to prepare optical limiters. However, these rely on nonlinear scattering,[117] rather than on nonlinear absorption.[118] The nonlinear scattering of graphene dispersions[116] is based on the avalanche ionization of carbon when interacting with an incident laser pulse, and subsequent bubble formation in the solvent due to the heat released by expanding

https://doi.org/10.1021/acsnano.1c04937
ACS Nano 2022, 16, 3613−3624

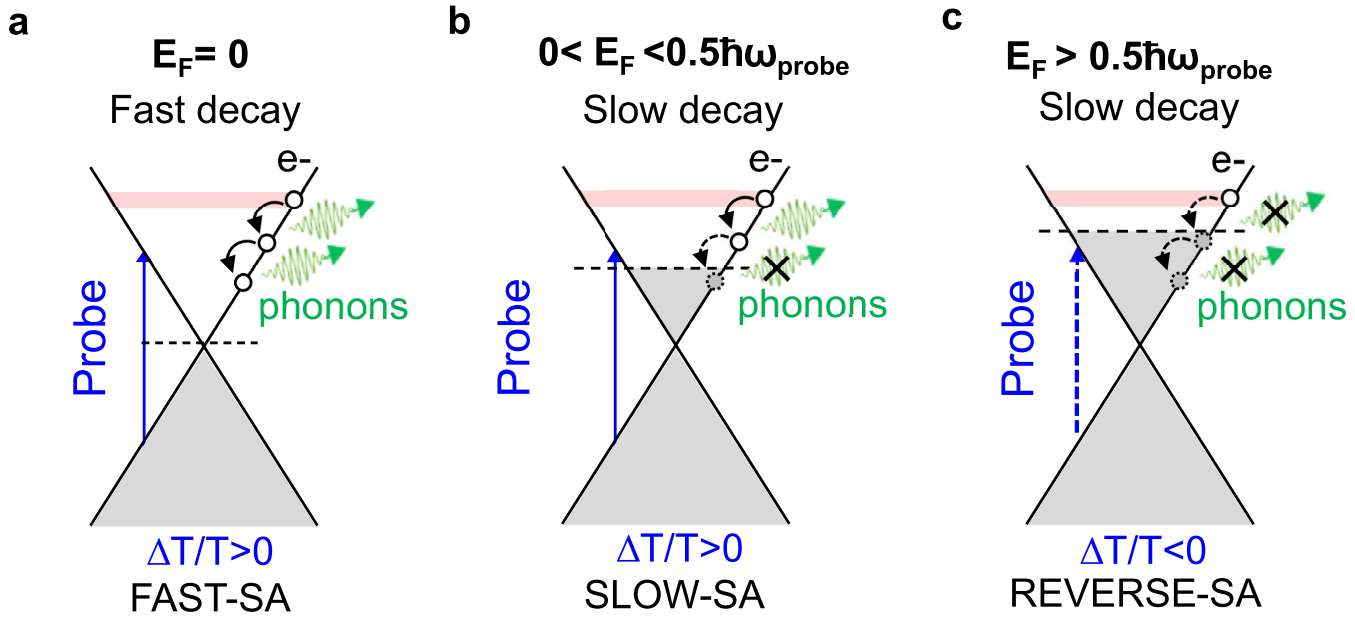

Figure 6. (a–c) Sketch of interband absorption of a NIR probe pulse (vertical blue arrow) within the SLG Dirac cones populated at equilibrium up to E_F (gray filling). The pump pulse perturbs the probe absorption by promoting e from VB to CB (red filling), which then relax through emission of optical phonons (downward black arrows). The three sketches correspond to (a) E_F at the Dirac point, (b,c) moderate *n*-doping with E_F (b) below and (c) above the threshold for interband probe absorption. By increasing E_F, optical phonon emission is quenched (dashed downward arrows) and relaxation becomes slower. Above the threshold for interband absorption of the probe (dashed vertical blue arrow), photoexcitation results in $\Delta T/T < 0$, leading to reverse saturable absorption, consisting in an increased absorption upon increasing illumination.

microplasmas.[115,116] The 10 ps PA lifetime of the nonlinear absorption of highly doped SLG is 10 times shorter than the typical time scales for thermal effects and bubbling of graphene dispersions, which are of the order of 100 ps,[115] allowing the application to lasers with shorter pulse duration. The nonlinear absorption in SLG is not related to a specific absorption resonance. Thus, it covers a broad spectral range, as shown in Figure 3b, where for $|E_F| = 600$ meV we detect PA for photon energies in the range 0.729 to 1.127 eV. The SA to reverse SA transition could be used for all-optical logic gates.[119] Gate-dependent effects on cooling dynamics are also important for the design of transceivers for data communication.[3] E.g., ref 120 showed that longer cooling times give larger photocurrent.

CONCLUSIONS

We demonstrated that electrostatic tuning of the non-equilibrium optical response of SLG results in changes of amplitude, sign, and recovery dynamics of $\Delta T/T$. Increasing E_F quenches emission of optical phonons, i.e., of the fastest intrinsic relaxation channel for SLG hot charge carriers. The ability to tune E_F above the threshold for Pauli blocking of interband absorption of NIR light results in photoinduced absorption in SLG, because of pump-induced unblocking of interband transitions for the probe. Our results anticipate the use of voltage-controlled SLG for nonequilibrium optoelectronic devices as gate tunable optical elements, which can behave either as fast, slow, or reverse SA.

METHODS

High-Sensitivity Transient Absorption Microscopy. The setup for pump–probe experiments comprises a mode-locked Er-doped fiber oscillator (Toptica Photonics, FemtoFiberPro), emitting 150 fs pulses at 0.8 eV (1550 nm) at 40 MHz repetition rate. The oscillator feeds two Er-doped fiber amplifiers (EDFAs) each generating 70 fs pulses at 0.8 eV with 300 mW average power. The output of the first EDFA is attenuated to obtain pump pulses with 1 mW maximum average power. The second EDFA feeds a highly nonlinear optical fiber that produces a supercontinuum tunable between 0.729 and 1.240 eV, which serves as probe pulse. The pump and probe pulses, synchronized by a computer-controlled optical delay line and collinearly recombined by a dichroic beam splitter, are focused on the sample over spots of ~25 μm radius. The portion of the probe transmitted by the sample, spectrally selected by a monochromator with a bandwidth ~5 nm, is detected by an amplified InGaAs photodiode (bandpass 4.5 MHz, gain 10^4) and analyzed by a lock-in amplifier (Zurich Instruments HF). Pump and probe pulses have perpendicular polarizations and a linear polarizer is used to filter out the pump light scattered from the sample. The pump pulse is modulated at 1 MHz by an acousto-optic modulator, resulting in a $\Delta T(t)/T$ sensitivity of the order of 10^{-7}, for an integration time of 300 ms. From the FWHM of the instrumental response function, we estimate an overall temporal resolution ~100 fs. The absorbed photon density is in the range $2–3 \times 10^{12}$cm^{-2} (depending on E_F), as calculated from incident fluence and sample transmission.

Simulation of Differential Transmission Dynamics. To model the time-evolution of the differential transmission we assume that, on the time-scale given by the time-resolution of the experiment (100 fs), e in both CB and VB are thermalized at the same T_e, and reach a common $\mu_c(t)$, such that the e energy distribution is a HFD. $\mu_c(t)$ is calculated at each instant in time, as it depends on T_e and is fixed by the condition that the carrier density, defined as[94] $n = \int_{-\infty}^{+\infty} d\varepsilon \nu(\varepsilon)[1 + \exp((\varepsilon - \mu)/k_B T)]^{-1}$, with $\nu(\varepsilon)$ the electronic density of states in SLG,[122] is constant.[94] As for refs 98 and 121, we can write the following EOMs for T_e and phonon occupations:

https://doi.org/10.1021/acsnano.1c04937
ACS Nano 2022, 16, 3613–3624

$$\frac{dT_e(t)}{dt} = -\frac{R_\Gamma(t)\hbar\omega_\Gamma + R_K(t)\hbar\omega_K}{c_e(t) + c_h(t)},$$
$$\frac{dn_\Gamma(t)}{dt} = \frac{R_\Gamma(t)}{M_\Gamma} - \frac{n_\Gamma(t) - n_\Gamma^{(0)}}{\tau_{ph}},$$
$$\frac{dn_K(t)}{dt} = \frac{R_K(t)}{M_K} - \frac{n_K(t) - n_K^{(0)}}{\tau_{ph}}. \quad (1)$$

Here, $n_\Gamma(t)$ and $n_K(t)$ are the occupations of the optical phonon modes at Γ and K, with energy $\hbar\omega_\Gamma \sim 0.196$ eV and $\hbar\omega_K \sim 0.161$ eV,[100] respectively, as these have the strongest electron−phonon coupling.[100] The parameter τ_{ph} is the finite optical phonon lifetime, via relaxation into acoustic phonons due nonlinearities of the lattice,[65] until global thermal equilibrium with densities $n_\Gamma^{(0)}$, $n_K^{(0)}$ is reached. We find good agreement between theory and experiment for $\tau_{ph} \sim 1.2$ ps, consistent with ref 65. The constant coefficients M_Γ, M_K correspond to the number of phonon modes in an annular region between the minimum and maximum energy that can be exchanged with e.[98,121] The time-dependent parameters $c_e(t)$ and $c_h(t)$ are the heat capacities of e in CB and h in VB, respectively. The time-dependent parameters $R_\Gamma(t)$ and $R_K(t)$ are electronic relaxation rates per unit area, due to phonon emission and absorption, proportional to a Boltzmann scattering integral.[98,121]

In line with our assumption that, on the time-scale probed by our experiments, a common $\mu_c(t)$ is established between CB and VB, the heat capacities are calculated separately in the two bands, (i.e., T_e variations are decoupled from interband transitions) and only intraband transitions are included in the relaxation rates. The initial $T_e(0)$, following the pump pulse, is estimated as for ref 37. The initial phonon populations $n_{\Gamma,K}(0)$ are evaluated at RT. The optical photoconductivity $\Delta\sigma(t) = \sigma(t) - \sigma(0)$[122] depends on $T_e(t)$ and $\mu_c(t)$. We use the Tinkham formula[123] to obtain the differential transmission.

AUTHOR INFORMATION

Corresponding Authors

Andrea C. Ferrari − *Cambridge Graphene Centre, University of Cambridge, Cambridge CB3 0FA, U.K.;* orcid.org/0000-0003-0907-9993; Email: acf26@eng.cam.ac.uk

Giulio Cerullo − *Dipartimento di Fisica, Politecnico di Milano, 20133 Milano, Italy; Istituto di Fotonica e Nanotecnologie, Consiglio Nazionale delle Ricerche, 20133 Milano, Italy;* orcid.org/0000-0002-9534-2702; Email: giulio.cerullo@polimi.it

Authors

Eva A. A. Pogna − *NEST, Istituto Nanoscienze-CNR and Scuola Normale Superiore, 56127 Pisa, Italy; Dipartimento di Fisica, Politecnico di Milano, 20133 Milano, Italy*

Andrea Tomadin − *Dipartimento di Fisica, Università di Pisa, 56127 Pisa, Italy*

Osman Balci − *Cambridge Graphene Centre, University of Cambridge, Cambridge CB3 0FA, U.K.;* orcid.org/0000-0003-2766-2197

Giancarlo Soavi − *Cambridge Graphene Centre, University of Cambridge, Cambridge CB3 0FA, U.K.; Institute of Solid State Physics, Friedrich Schiller University Jena, Jena 07743, Germany;* orcid.org/0000-0003-2434-2251

Ioannis Paradisanos − *Cambridge Graphene Centre, University of Cambridge, Cambridge CB3 0FA, U.K.*

Michele Guizzardi − *Dipartimento di Fisica, Politecnico di Milano, 20133 Milano, Italy*

Paolo Pedrinazzi − *L-NESS, Department of Physics, Politecnico di Milano, Como 22100, Italy*

Sandro Mignuzzi − *Cambridge Graphene Centre, University of Cambridge, Cambridge CB3 0FA, U.K.*

Klaas-Jan Tielrooij − *Catalan Institute of Nanoscience and Nanotechnology (ICN2), BIST & CSIC, Barcelona 08193, Spain;* orcid.org/0000-0002-0055-6231

Marco Polini − *Dipartimento di Fisica, Università di Pisa, 56127 Pisa, Italy; Istituto Italiano di Tecnologia, 16163 Genova, Italy*

Complete contact information is available at: https://pubs.acs.org/10.1021/acsnano.1c04937

Notes

The authors declare no competing financial interest.

ACKNOWLEDGMENTS

We thank A. Principi for useful discussions. We acknowledge funding from the European Union Graphene Flagship, ERC Grants Hetero2D, GSYNCOR, and CUHL, EPSRC Grants EP/K01711X/1, EP/K017144/1, EP/N010345/1, EP/L016087/1, EP/V000055/1, the German Research Foundation DFG (CRC 1375 NOA), the Daimler und Benz foundation, RYC fellowship No. RYC-2017-22330, IAE project PID2019-111673GB-I00, and the Severo Ochoa program from Spanish MINECO Grant No. SEV-2017-0706.

REFERENCES

(1) Ferrari, A. C.; Bonaccorso, F.; Fal'ko, V.; Novoselov, K. S.; Roche, S.; Bøggilg, P.; Borini, S.; Koppens, F. H. L.; Palermo, V.; Pugno, N. M.; Garrido, J. A.; Sordan, R.; Bianco, A.; Ballerini, L.; Prato, M.; Lidorikis, E.; Kivioja, J.; Marinelli, C.; Ryhänen, T.; Morpurgo, A.; et al. Science and Technology Roadmap for Graphene, Related Two-Dimensional Crystals, and Hybrid Systems. *Nanoscale* **2015**, *7*, 4598−4810.

(2) Bonaccorso, F.; Sun, Z.; Hasan, T.; Ferrari, A. C. Graphene Photonics and Optoelectronics. *Nat. Photonics* **2010**, *4*, 611−22.

(3) Romagnoli, M.; Sorianello, V.; Midrio, M.; Koppens, F. H. L.; Huyghebaert, C.; Neumaier, D.; Galli, P.; Templ, W.; D'Errico, A.; Ferrari, A. C. Graphene-Based Integrated Photonics for Next-Generation Datacom and Telecom. *Nat. Rev. Mater.* **2018**, *3*, 392−414.

(4) Du, X.; Skachko, I.; Barker, A.; Andrei, E. Y. Approaching Ballistic Transport in Suspended Graphene. *Nat. Nanotechnol.* **2008**, *3*, 491−5.

(5) Bolotin, K. I.; Sikes, J.; Jiang, Z.; Klima, M.; Fudenberg, G.; Hone, J.; Kim, P.; Stormer, H. L. Ultrahigh Electron Mobility in Suspended Graphene. *Solid State Commun.* **2008**, *146*, 351−5.

(6) Purdie, D. G.; Pugno, N. M.; Taniguchi, T.; Watanabe, K.; Ferrari, A. C.; Lombardo, A. Cleaning Interfaces in Layered Materials Heterostructures. *Nat. Commun.* **2018**, *9*, 5387.

(7) De Fazio, D.; Purdie, D. G.; Ott, A. K.; Braeuninger-Weimer, P.; Khodkov, T.; Goossens, S.; Taniguchi, T.; Watanabe, K.; Livreri, P.; Koppens, F. H. L.; Hofmann, S.; Goykhman, I.; Ferrari, A. C.; Lombardo, A. High-Mobility, Wet-Transferred Graphene Grown by Chemical Vapor Deposition. *ACS Nano* **2019**, *13*, 8926−35.

(8) Nair, R. R.; Blake, P.; Grigorenko, A. N.; Novoselov, K. S.; Booth, T. J.; Stauber, T.; Peres, N. M. R.; Geim, A. K. Fine Structure Constant Defines Visual Transparency of Graphene. *Science* **2008**, *320*, 1308.

(9) Pisana, S.; Lazzeri, M.; Casiraghi, C.; Novoselov, K. S.; Geim, A. K.; Ferrari, A. C.; Mauri, F. Breakdown of the Adiabatic Born-Oppenheimer Approximation in Graphene. *Nat. Mater.* **2007**, *6*, 198−201.

(10) Neto, A. H.; Guinea, F.; Peres, N. M. R.; Novoselov, K. S.; Geim, A. K. The Electronic Properties of Graphene. *Rev. Mod. Phys.* **2009**, *81*, 109.

(11) Ando, T.; Zheng, Y.; Suzuura, H. Dynamical Conductivity and Zero-Mode Anomaly in Honeycomb Lattices. *J. Phys. Soc. Jpn.* **2002**, *71*, 1318−24.
(12) Gusynin, V.; Sharapov, S.; Carbotte, J. Unusual Microwave Response of Dirac Quasiparticles in Graphene. *Phys. Rev. Lett.* **2006**, *96*, 256802.
(13) Horng, J.; Chen, C.-F.; Geng, B.; Girit, C.; Zhang, Y.; Hao, Z.; Bechtel, H. A.; Martin, M.; Zettl, A.; Crommie, M. F.; Shen, Y. R.; Wang, F. Drude Conductivity of Dirac Fermions in Graphene. *Phys. Rev. B* **2011**, *83*, 165113.
(14) Mak, K. F.; Ju, L.; Wang, F.; Heinz, T. F. Optical Spectroscopy of Graphene: from the Far Infrared to the Ultraviolet. *Solid State Commun.* **2012**, *152*, 1341−9.
(15) Mak, K. F.; Sfeir, M. Y.; Wu, Y.; Lui, C. H.; Misewich, J. A.; Heinz, T. F. Measurement of the Optical Conductivity of Graphene. *Phys. Rev. Lett.* **2008**, *101*, 196405.
(16) Liu, F.; Chong, Y. D.; Adam, S.; Polini, M. Gate-Tunable Coherent Perfect Absorption of Terahertz Radiation in Graphene. *2D Mater.* **2014**, *1*, 031001.
(17) Balci, O.; Kakenov, N.; Kocabas, C. Controlling Phase of Microwaves with Active Graphene Surfaces. *Appl. Phys. Lett.* **2017**, *110*, 161102.
(18) Wang, F.; Zhang, Y.; Tian, C.; Girit, C.; Zettl, A.; Crommie, M.; Shen, R. Gate-Variable Optical Transitions in Graphene. *Science* **2008**, *320*, 206−9.
(19) Liang, G.; Hu, X.; Yu, X.; Shen, Y.; Li, L. H.; Davies, A. G.; Linfield, E. H.; Liang, H. K.; Zhang, Y.; Yu, S. F.; Wang, Q. J. Integrated Terahertz Graphene Modulator with 100% Modulation Depth. *ACS Photonics* **2015**, *2*, 1559−1566.
(20) Mao, Q.; Wen, Q. Y.; Tian, W.; Wen, T. L.; Chen, Z.; Yang, Q. H.; Zhang, H. W. High-Speed and Broadband Terahertz Wave Modulators Based on Large-Area Graphene Field-Effect Transistors. *Opt. Lett.* **2014**, *39*, 5649−52.
(21) Li, Q.; Tian, Z.; Zhang, X.; Singh, R.; Du, L.; Gu, L.; Han, J.; Zhang, W. Active Graphene-Silicon Hybrid Diode for Terahertz Waves. *Nat. Commun.* **2015**, *6*, 7082.
(22) Kakenov, N.; Balci, O.; Takan, T.; Ozkan, V. A.; Altan, H.; Kocabas, C. Observation of Gate-Tunable Coherent Perfect Absorption of Terahertz Radiation in Graphene. *ACS Photonics* **2016**, *3*, 1531−5.
(23) Di Gaspare, A.; Pogna, E. A. A.; Salemi, L.; Balci, O.; Cadore, A. R.; Shinde, S. M.; Li, L.; di Franco, C.; Davies, A. G.; Linfield, E. H.; Ferrari, A. C.; Scamarcio, G.; Vitiello, M. S. Tunable, Grating Gated, Graphene on Polyimide Terahertz Modulators. *Adv. Fun. Mater.* **2021**, *31*, 2008039.
(24) Yao, Y.; Kats, M. A.; Shankar, R.; Song, Y.; Kong, J.; Loncar, M.; Capasso, F. Wide Wavelength Tuning of Optical Antennas on Graphene with Nanosecond Response Time. *Nano Lett.* **2014**, *14*, 214−9.
(25) Giambra, M. A.; Sorianello, V.; Miseikis, V.; Marconi, S.; Montanaro, A.; Galli, P.; Pezzini, S.; Coletti, C.; Romagnoli, M. High-Speed Double Layer Graphene Electro-Absorption Modulator on SOI Waveguide. *Opt. Express* **2019**, *27*, 20145−55.
(26) Zeng, B.; Huang, Z.; Singh, A.; Yao, Y.; Azad, A. K.; Mohite, A. D.; Taylor, A. J.; Smith, D. R.; Chen, H. -T. Hybrid Graphene Metasurfaces for High-Speed Mid-Infrared Light Modulation and Single-Pixel Imaging. *Light Sci. Appl.* **2018**, *7*, 51.
(27) Dalir, H.; Xia, Y.; Wang, Y.; Zhang, X. Athermal Broadband Graphene Optical Modulator with 35 GHz Speed. *ACS Photonics* **2016**, *3*, 1564−8.
(28) Polat, E. O.; Kocabas, C. Broadband Optical Modulators Based on Graphene Supercapacitors. *Nano Lett.* **2013**, *13*, 5851−7.
(29) Phare, C. T.; Lee, Y. D.; Cardenas, J.; Lipson, M. Graphene Electro-Optic Modulator with 30 GHz Bandwidth. *Nat. Photonics* **2015**, *9*, 511−4.
(30) Liu, M.; Yin, X.; Ulin-Avila, E.; Geng, B.; Zentgraf, T.; Ju, L.; Wang, F.; Zhang, X. A Graphene-Based Broadband Optical Modulator. *Nature* **2011**, *474*, 64−7.
(31) Sorianello, V.; Midrio, M.; Contestabile, G.; Asselberghs, I.; Van Campenhout, J.; Huyghebaert, C.; Goykhman, I.; Ott, A. K.; Ferrari, A. C.; Romagnoli, M. Graphene-Silicon Phase Modulators with Gigahertz Bandwidth. *Nat. Photonics* **2018**, *12*, 40−4.
(32) Midrio, M.; Boscolo, S.; Moresco, M.; Romagnoli, M.; De Angelis, C.; Locatelli, A.; Capobianco, A.-D. Graphene-Assisted Critically-Coupled Optical Ring Modulator. *Opt. Express* **2012**, *20*, 23144−55.
(33) Ye, S.; Wang, Z.; Tang, L.; Zhang, Y.; Lu, R.; Liu, Y. Electro-Absorption Optical Modulator Using Dual-Graphene-on-Graphene Configuration. *Opt. Express* **2014**, *22*, 26173−80.
(34) Liu, J.; Khan, Z. U.; Wang, C.; Zhang, H.; Sarjoghian, S. Review of Graphene Modulators from the Low to the High Figure of Merits. *J. Phys. D: Appl. Phys.* **2020**, *53*, 233002.
(35) Li, M.; Ling, J.; He, Y.; Javid, U. A.; Xue, S.; Lin, Q. Lithium Niobate Photonic-Crystal Electro-Optic Modulator. *Nat. Commun.* **2020**, *11*, 4123.
(36) Rahim, A.; Hermans, A.; Wohlfeil, B.; Petousi, D.; Kuyken, B.; Van Thourhout, D.; Baets, R. G. Taking Silicon Photonics Modulators to a Higher Performance Level: State-of-the-Art and a Review of New Technologies. *Adv. Photon.* **2021**, *3*, 024003.
(37) Soavi, G.; Wang, G.; Rostami, H.; Purdie, D. G.; De Fazio, D.; Ma, T.; Luo, B.; Wang, J.; Ott, A. K.; Yoon, D.; Bourelle, S. A.; Muench, J. E.; Goykhman, I.; Dal Conte, S.; Celebrano, M.; Tomadin, A.; Polini, M.; Cerullo, G.; Ferrari, A. C. Broadband, Electrically Tunable Third-Harmonic Generation in Graphene. *Nat. Nanotechnol.* **2018**, *13*, 583−8.
(38) Yoshikawa, N.; Tamaya, T.; Tanaka, K. High-Harmonic Generation in Graphene Enhanced by Elliptically Polarized Light Excitation. *Science* **2017**, *356*, 736−8.
(39) Hafez, H. A.; Kovalev, S.; Deinert, J.-C.; Mics, Z.; Green, B.; Awari, N.; Chen, M.; Germanskiy, S.; Lehnert, U.; Teichert, J.; Wang, Z.; Tielrooij, K.-J.; Liu, Z.; Chen, Z.; Narita, A.; Mullen, K.; Bonn, M.; Gensch, M.; Turchinovich, D. Extremely Efficient Terahertz High-Harmonic Generation in Graphene by Hot Dirac Fermions. *Nature* **2018**, *561*, 507.
(40) Kovalev, S.; Hafez, H. A.; Tielrooij, K.-J.; Deinert, J.-C.; Ilyakov, I.; Awari, N.; Alcaraz, D.; Soundarapandian, K.; Saleta, D.; Germanskiy, S.; Chen, M.; Bawatna, M.; Green, B.; Koppens, F. H.; Mittendorff, M.; Bonn, M.; Gensch, M.; Turchinovich, D. Electrical Tunability of Terahertz Nonlinearity in Graphene. *Sci. Adv.* **2021**, *7*, No. eabf9809.
(41) Jiang, T.; Huang, D.; Cheng, J.; Fan, X.; Zhang, Z.; Shan, Y.; Yi, Y.; Dai, Y.; Shi, L.; Liu, K.; Zeng, C.; Zi, J.; Sipe, J. E.; Shen, Y.-R.; Liu, W.-T.; Wu, S. Gate-Tunable Third-Order Nonlinear Optical Response of Massless Dirac Fermions in Graphene. *Nat. Photonics* **2018**, *12*, 430−6.
(42) Buchalter, B.; Meredith, G. R. Third-Order Optical Susceptibility of Glasses Determined by Third Harmonic Generation. *Appl. Opt.* **1982**, *21*, 3221−4.
(43) Rosa, H. G.; Ho, Y. W.; Verzhbitskiy, I.; Rodrigues, M. J. F. L.; Taniguchi, T.; Watanabe, K.; Eda, G.; Pereira, V. M.; Gomes, J. C. V. Characterization of the Second- and Third-Harmonic Optical Susceptibilities of Atomically Thin Tungsten Diselenide. *Sci. Rep.* **2018**, *8*, 10035.
(44) Sun, Z.; Hasan, T.; Torrisi, F.; Popa, D.; Privitera, G.; Wang, F.; Bonaccorso, F.; Basko, D. M.; Ferrari, A. C. Graphene Mode-Locked Ultrafast Laser. *ACS Nano* **2010**, *4*, 803−10.
(45) Yu, S.; Wu, X.; Chen, K.; Chen, B.; Guo, X.; Dai, D.; Tong, L.; Liu, W.; Shen, Y. R. All-Optical Graphene Modulator Based on Optical Kerr Phase Shift. *Optica* **2016**, *3*, 541−4.
(46) Peres, N. M. R.; Bludov, Y. V.; Santos, J. E.; Jauho, A.-J.; Vasilevskiy, M. I. Optical Bistability of Graphene in the Terahertz Range. *Phys. Rev. B* **2014**, *90*, 125425.
(47) Sadeghi, M.; Ahmadi, V. Multilayer Graphene Based Optical Bistability. *J. Opt. Soc. Am. B* **2018**, *35*, 528−32.
(48) Abraham, E.; Smith, S. D. Optical Bistability and Related Devices. *Rep. Prog. Fisica* **1982**, *45*, 815−85.

https://doi.org/10.1021/acsnano.1c04937
ACS Nano 2022, 16, 3613−3624

(49) Alexander, K.; Savostianova, N. A.; Mikhailov, S. A.; Kuyken, B.; Van Thourhout, D. Electrically Tunable Optical Nonlinearities in Graphene-Covered SiN Waveguides Characterized by Four-Wave Mixing. *ACS Photonics* **2017**, *4*, 3039−44.
(50) Frenzel, A. J.; Lui, C. H.; Shin, Y. C.; Kong, J.; Gedik, N. Semiconducting-to-Metallic Photoconductivity Crossover and Temperature-Dependent Drude Weight in Graphene. *Phys. Rev. Lett.* **2014**, *113*, 056602.
(51) Shi, S.-F.; Tang, T. T.; Zeng, B.; Ju, L.; Zhou, Q.; Zettl, A.; Wang, F. Controlling Graphene Ultrafast Hot Carrier Response from Metal-Like to Semiconductor-Like by Electrostatic Gating. *Nano Lett.* **2014**, *14*, 1578−82.
(52) Hafez, H. A.; Lévesque, P. L.; Al-Naib, I.; Dignam, M. M.; Chai, X.; Choubak, S.; Desjardins, P.; Martel, R.; Ozaki, T. Intense Terahertz Field Effects on Photoexcited Carrier Dynamics in Gated Graphene. *Appl. Phys. Lett.* **2015**, *107*, 251903.
(53) Lin, K. C.; Li, M. Y.; Ling, D. C.; Chi, C. C.; Chen, J. C. Evolution of Hot Carrier Dynamics in Graphene with the Fermi Level Tuned Across the Dirac Point. *Phys. Rev. B* **2015**, *91*, 125440.
(54) Mikhailov, S. A. Theory of the Strongly Nonlinear Electrodynamic Response of Graphene: A Hot Electron Model. *Phys. Rev. B* **2019**, *100*, 115416.
(55) Koppens, F. H. L.; Mueller, T.; Avouris, Ph.; Ferrari, A. C.; Vitiello, M. S.; Polini, M. Photodetectors Based on Graphene, Other Two-Dimensional Materials and Hybrid Systems. *Nat. Nanotechnol.* **2014**, *9*, 780−93.
(56) Dawlaty, J. M.; Shivaraman, S.; Chandrashekhar, M.; Rana, F.; Spencer, M. G. Measurement of Ultrafast Carrier Dynamics in Epitaxial Graphene. *Appl. Phys. Lett.* **2008**, *92*, 042116.
(57) Sun, D.; Wu, Z.-K.; Divin, C.; Li, X.; Berger, C.; de Heer, W. A.; First, P. N.; Norris, T. B. Ultrafast Relaxation of Excited Dirac Fermions in Epitaxial Graphene Using Optical Differential Transmission Spectroscopy. *Phys. Rev. Lett.* **2008**, *101*, 157402.
(58) Breusing, M.; Kuehn, S.; Winzer, T.; Malic, E.; Milde, F.; Severin, N.; Rabe, J. P.; Ropers, C.; Knorr, A.; Elsaesser, T. Ultrafast Nonequilibrium Carrier Dynamics in a Single Graphene Layer. *Phys. Rev. B* **2011**, *83*, 153410.
(59) Kotov, V. N.; Uchoa, B.; Pereira, V. M.; Guinea, F.; Neto, A. C. Electron-Electron Interactions in Graphene: Current Status and Perspectives. *Rev. Mod. Phys.* **2012**, *84*, 1067.
(60) Brida, D.; Tomadin, A.; Manzoni, C.; Kim, Y. J.; Lombardo, A.; Milana, S.; Nair, R. R.; Novoselov, K. S.; Ferrari, A. C.; Cerullo, G.; Polini, M. Ultrafast Collinear Scattering and Carrier Multiplication in Graphene. *Nat. Commun.* **2013**, *4*, 1987.
(61) Cerullo, G.; Manzoni, C.; Lüer, L.; Polli, D. Time-Resolved Methods in Biophysics. 4. Broadband Pump-Probe Spectroscopy System with Sub-20 fs Temporal Resolution for the Study of Energy Transfer Processes in Photosynthesis. *Photochem. Photobiol. Sci.* **2007**, *6*, 135−144.
(62) Lazzeri, M.; Piscanec, S.; Mauri, F.; Ferrari, A. C.; Robertson, J. Electron Transport and Hot Phonons in Carbon Nanotubes. *Phys. Rev. Lett.* **2005**, *95*, 236802.
(63) Tomadin, A.; Brida, D.; Cerullo, G.; Ferrari, A. C.; Polini, M. Nonequilibrium Dynamics of Photoexcited Electrons in Graphene: Collinear Scattering, Auger Processes, and the Impact of Screening. *Phys. Rev. B* **2013**, *88*, 035430.
(64) Pogna, E. A. A.; Jia, X.; Principi, A.; Block, A.; Banszerus, L.; Zhang, J.; Liu, X.; Sohier, T.; Forti, S.; Soundarapandian, K.; Terrés, B.; Mehew, J. D.; Trovatello, C.; Coletti, C.; Koppens, F. H. L.; Bonn, M.; Wang, H. I.; van Hulst, N.; Verstraete, M. J.; Peng, H.; Liu, Z.; et al. Hot-Carrier Cooling in High-Quality Graphene Is Intrinsically Limited by Optical Phonons. *ACS Nano* **2021**, *15*, 11285−11295.
(65) Bonini, N.; Lazzeri, M.; Marzari, N.; Mauri, F. Phonon Anharmonicities in Graphite and Graphene. *Phys. Rev. Lett.* **2007**, *99*, 176802.
(66) Tielrooij, K.-J.; Hesp, N. C. H.; Principi, A.; Lundeberg, M. B.; Pogna, E. A. A.; Banszerus, L.; Mics, Z.; Massicotte, M.; Schmidt, P.; Davydovskaya, D.; Purdie, D. G.; Goykhman, I.; Soavi, G.; Lombardo, A.; Watanabe, K.; Taniguchi, K.; Bonn, M.; Turchinovich, D.; Stampfer, C.; Ferrari, A. C.; et al. Out-of-Plane Heat Transfer in van der Waals Stacks through Electron-Hyperbolic Phonon Coupling. *Nat. Nanotechnol.* **2018**, *13*, 41−6.
(67) Graham, M. W.; Shi, S.-F.; Ralph, D. C.; Park, J.; McEuen, P. L. Photocurrent Measurements of Supercollision Cooling in Graphene. *Nat. Phys.* **2013**, *9*, 103−8.
(68) Betz, A. C.; Jhang, H.; Pallecchi, E.; Ferreira, R.; Féve, G.; Berroir, J.-M.; Plaçais, B. Supercollision Cooling in Undoped Graphene. *Nat. Phys.* **2013**, *9*, 109−12.
(69) Song, J. C. W.; Reizer, M. Y.; Levitov, L. S. Disorder-Assisted Electron-Phonon Scattering and Cooling Pathways in Graphene. *Phys. Rev. Lett.* **2012**, *109*, 106602.
(70) Alencar, T. V.; Silva, M. G.; Malard, L. M.; de Paula, A. M. Defect-Induced Supercollision Cooling of Photoexcited Carriers in Graphene. *Nano Lett.* **2014**, *14*, 5621−4.
(71) Das, A.; Pisana, S.; Chakraborty, B.; Piscanec, S.; Saha, S. K.; Waghmare, U. V.; Novoselov, K. S.; Krishnamurthy, H. R.; Geim, A. K.; Ferrari, A. C.; Sood, A. K. Monitoring Dopants by Raman Scattering in an Electrochemically Top-Gated Graphene Transistor. *Nat. Nanotechnol.* **2008**, *3*, 210−5.
(72) Li, X.; Cai, W.; An, J.; Kim, S.; Nah, J.; Yang, D.; Piner, R.; Velamakanni, A.; Jung, I.; Tutuc, E.; Banerjee, S. K.; Colombo, L.; Ruoff, R. S. Large-Area Synthesis of High-Quality and Uniform Graphene Films on Copper Foils. *Science* **2009**, *324*, 1312−4.
(73) Soavi, G.; Wang, G.; Rostami, H.; Tomadin, A.; Balci, O.; Paradisanos, I.; Pogna, E. A. A.; Cerullo, G.; Lidorikis, E.; Polini, M.; Ferrari, A. C. Hot Electrons Modulation of Third-Harmonic Generation in Graphene. *ACS Photonics* **2019**, *6*, 2841−9.
(74) Lagatsky, A. A.; Sun, Z.; Kulmala, T. S.; Sundaram, R. S.; Milana, S.; Torrisi, F.; Antipov, O. L.; Lee, Y.; Ahn, J. H.; Brown, C. T. A.; Sibbett, W.; Ferrari, A. C. 2μm Solid-State Laser Mode-Locked by Single-Layer Graphene. *Appl. Phys. Lett.* **2013**, *102*, 013113−013113.
(75) Ferrari, A. C.; Meyer, J. C.; Scardaci, V.; Casiraghi, C.; Lazzeri, M.; Mauri, F.; Piscanec, S.; Jiang, D.; Novoselov, K. S.; Roth, S.; Geim, A. K. Raman Spectrum of Graphene and Graphene Layers. *Phys. Rev. Lett.* **2006**, *97*, 187401.
(76) Ferrari, A. C.; Robertson, J. Interpretation of Raman Spectra of Disordered and Amorphous Carbon. *Phys. Rev. B* **2000**, *61*, 14095.
(77) Ferrari, A. C.; Basko, D. M. Raman Spectroscopy as a Versatile Tool for Studying the Properties of Graphene. *Nat. Nanotechnol.* **2013**, *8*, 235−46.
(78) Basko, D. M.; Piscanec, S.; Ferrari, A. C. Electron-Electron Interactions and Doping Dependence of the Two-Phonon Raman Intensity in Graphene. *Phys. Rev. B* **2009**, *80*, 165413.
(79) Bruna, M.; Ott, A. K.; Ijäs, M.; Yoon, D.; Sassi, U.; Ferrari, A. C. Doping Dependence of the Raman Spectrum of Defected Graphene. *ACS Nano* **2014**, *8*, 7432−41.
(80) Mohiuddin, T. M. G.; Lombardo, A.; Nair, R. R.; Bonetti, A.; Savini, G.; Jalil, R.; Bonini, N.; Basko, D. M.; Galiotis, C.; Marzari, N.; Novoselov, K. S.; Geim, A. K.; Ferrari, A. C. Uniaxial Strain in Graphene by Raman Spectroscopy: G Peak Splitting, Grüneisen Parameters, and Sample Orientation. *Phys. Rev. B* **2009**, *79*, 205433.
(81) Yoon, D.; Son, Y.-W.; Cheong, H. Strain-Dependent Splitting of the Double-Resonance Raman Scattering Band in Graphene. *Phys. Rev. Lett.* **2011**, *106*, 155502.
(82) Das, A.; Chakraborty, B.; Piscanec, S.; Pisana, S.; Sood, A. K.; Ferrari, A. C. Phonon Renormalization in Doped Bilayer Graphene. *Phys. Rev. B* **2009**, *79*, 155417.
(83) Ye, J.; Inoue, S.; Kobayashi, K.; Kasahara, Y.; Yuan, H. T.; Shimotani, H.; Iwasa, Y. Liquid-Gated Interface Superconductivity on an Atomically Flat Film. *Nat. Mater.* **2010**, *9*, 125−128.
(84) Du, H.; Lin, X.; Xu, Z.; Chu, D. Electric Double-Layer Transistors: a Review of Recent Progress. *J. Mater. Sci.* **2015**, *50*, 5641−73.
(85) Geim, A. K.; Novoselov, K. S. The Rise of Graphene. *Nat. Mater.* **2007**, *6*, 183−91.

https://doi.org/10.1021/acsnano.1c04937
ACS Nano 2022, 16, 3613−3624

(86) Xu, H.; Zhang, Z.; Wang, Z.; Wang, S.; Liang, X.; Peng, L.-M. Quantum Capacitance Limited Vertical Scaling of Graphene Field-Effect Transistor. *ACS Nano* **2011**, *5*, 2340−7.
(87) Casiraghi, C.; Hartschuh, A.; Lidorikis, E.; Qian, H.; Harutyunyan, H.; Gokus, T.; Novoselov, K. S.; Ferrari, A. C. Rayleigh Imaging of Graphene and Graphene Layers. *Nano Lett.* **2007**, *7*, 2711−7.
(88) Specification Sheet. https://www.sigmaaldrich.com/IT/it/specification-sheet/ALDRICH/727679 (accessed July, 2021).
(89) Casiraghi, C.; Pisana, S.; Novoselov, K. S.; Geim, A. K.; Ferrari, A. C. Raman Fingerprint of Charged Impurities in Graphene. *Appl. Phys. Lett.* **2007**, *91*, 233108.
(90) Martin, J.; Akerman, N.; Ulbricht, G.; Lohmann, T.; Smet, J. H.; von Klitzing, K.; Yacoby, A. Observation of Electron-Hole Puddles in Graphene Using a Scanning Single-Electron Transistor. *Nat. Phys.* **2008**, *4*, 144−8.
(91) Adam, S.; Hwang, E.; Galitski, V.; Das Sarma, S. A Self-Consistent Theory for Graphene Transport. *Proc. Natl. Acad. Sci. U. S. A.* **2007**, *104*, 18392−7.
(92) Li, Z.; Henriksen, E. A.; Jiang, Z.; Hao, Z.; Martin, M. C.; Kim, P.; Stormer, H. L.; Basov, D. N. Dirac Charge Dynamics in Graphene by Infrared Spectroscopy. *Nat. Phys.* **2008**, *4*, 532−5.
(93) Katayama, I.; Inoue, K.; Arashida, Y.; Wu, Y.; Yang, H.; Inoue, T.; Chiashi, S.; Maruyama, S.; Nagao, T.; Kitajima, M.; Takeda, J. Ultrafast Optical Modulation of Dirac Electrons in Gated Single-Layer Graphene. *Phys. Rev. B* **2020**, *101*, 245208.
(94) Kittel, C. *Introduction to Solid State Physics*; Wiley New York: New York, 1996.
(95) Marini, A.; Cox, J. D.; García de Abajo, F. J. Theory of Graphene Saturable Absorption. *Phys. Rev. B* **2017**, *95*, 125408.
(96) Yao, J.; Zhao, X.; Yan, X.-Q.; Kong, X.-T.; Gao, C.; Chen, X.-D.; Chen, Y.; Liu, Z.-B.; Tian, J. G. Making Transient Optical Reflection of Graphene Polarization Dependent. *Opt. Express* **2015**, *23*, 24177−24188.
(97) Malard, L. M.; Mak, K. F.; Castro Neto, A. H.; Peres, N. M. R.; Heinz, T. F. Observation of Intra- and Inter-Band Transitions in the Transient Optical Response of Graphene. *New J. Phys.* **2013**, *15*, 015009.
(98) Rana, F.; George, P. A.; Strait, J. H.; Dawlaty, J.; Shivaraman, S.; Chandrashekhar, M.; Spencer, M. G. Carrier Recombination and Generation Rates for Intravalley and Intervalley Phonon Scattering in Graphene. *Phys. Rev. B* **2009**, *79*, 115447.
(99) Song, Y.-W.; Jang, S.-Y.; Han, W.-S.; Bae, M.-K. Graphene Mode-Lockers for Fiber Lasers Functioned with Evanescent Field Interaction. *Appl. Phys. Lett.* **2010**, *96*, 051122.
(100) Piscanec, S.; Lazzeri, M.; Mauri, F.; Ferrari, A. C.; Robertson, J. Kohn Anomalies and Electron-Phonon Interactions in Graphite. *Phys. Rev. Lett.* **2004**, *93*, 185503.
(101) RP Photonics logo Encyclopedia. https://www.rp-photonics.com/saturable_absorbers.html (accessed April, 2021).
(102) Zhang, F.; Han, S.; Liu, Y.; Wang, Z.; Xu, X. Dependence of the Saturable Absorption of Graphene upon Excitation Photon Energy. *Appl. Phys. Lett.* **2015**, *106*, 091102.
(103) Spühler, G.; Weingarten, K. J.; Grange, R.; Krainer, L.; Haiml, M.; Liverini, V.; Golling, M.; Schön, S.; Keller, U. Semiconductor Saturable Absorber Mirror Structures with Low Saturation Fluence. *Appl. Phys. B: Laser Opt.* **2005**, *81*, 27−32.
(104) Sheng, Q.-W.; Feng, M.; Xin, W.; Guo, H.; Han, T.-Y.; Li, Y.-G.; Liu, Y.-G.; Gao, F.; Song, F.; Liu, Z.-B.; Tian, J.-G. Tunable Graphene Saturable Absorber with Cross Absorption Modulation for Mode-Locking in Fiber Laser. *Appl. Phys. Lett.* **2014**, *105*, 041901.
(105) Popa, D.; Sun, Z.; Torrisi, F.; Hasan, T.; Wang, F.; Ferrari, A. C. Sub 200 fs Pulse Generation from a Graphene Mode-Locked Fiber Laser. *Appl. Phys. Lett.* **2010**, *97*, 203106.
(106) Sun, Z.; Popa, D.; Hasan, T.; Torrisi, F.; Wang, F.; Kelleher, E. J. R.; Travers, J. C.; Nicolosi, V.; Ferrari, A. C. A Stable, Wideband Tunable, Near Transform-Limited, Graphene-Mode-Locked, Ultrafast Laser. *Nano Res.* **2010**, *3*, 653−60.
(107) Popa, D.; Sun, Z.; Hasan, T.; Torrisi, F.; Wang, F.; Ferrari, A. C. Graphene Q-Switched, Tunable Fiber Laser. *Appl. Phys. Lett.* **2011**, *98*, 073106.
(108) Xie, G. Q.; Ma, J.; Lv, P.; Gao, W. L.; Yuan, P.; Qian, L. J.; Yu, H. H.; Zhang, H. J.; Wang, J. Y.; Tang, D. Y. Graphene Saturable Absorber for Q-Switching and Mode Locking at 2 μm Wavelength. *Opt. Mater. Express* **2012**, *2*, 878−83.
(109) Keller, U. Recent Developments in Compact Ultrafast Lasers. *Nature* **2003**, *424*, 831−8.
(110) Keller, U.; Weingarten, K. J.; Kärtner, F. X.; Kopf, D.; Braun, B.; Jung, I. D.; Fluck, R.; Honninger, C.; Matuschek, N.; Aus der Au, J. Semiconductor Saturable Absorber Mirrors (SESAM's) for Femtosecond to Nanosecond Pulse Generation in Solid-State Lasers. *IEEE J. Sel. Top. Quant.* **1996**, *2*, 435−53.
(111) Paschotta, R.; Keller, U. Passive Mode Locking with Slow Saturable Absorbers. *Appl. Phys. B: Laser Opt.* **2001**, *73*, 653−62.
(112) Kartner, F. X.; Jung, I. D.; Keller, U. Soliton Mode-Locking with Saturable Absorbers. *IEEE J. Sel. Top. Quantum Electron.* **1996**, *2*, 540−56.
(113) Band, Y. B. *Optical Properties and Applications of Reverse Saturable Absorbers*; Springer: Boston, MA, 1986.
(114) Harter, D. J.; Shand, M. L.; Band, Y. B. Power/Energy Limiter Using Reverse Saturable Absorption. *J. Appl. Phys.* **1984**, *56*, 865.
(115) Wang, J.; Blau, W. J. Solvent Effect on Optical Limiting Properties of Single-Walled Carbon Nanotube Dispersions. *J. Phys. Chem. C* **2008**, *112*, 2298−303.
(116) Wang, J.; Hernandez, Y.; Lotya, M.; Coleman, J.; Blau, W. J. Broadband Nonlinear Optical Response of Graphene Dispersions. *Adv. Mater.* **2009**, *21*, 2430−5.
(117) Tutt, L. W.; Boggess, T. F. A Review of Optical Limiting Mechanisms and Devices Using Organics, Fullerenes, Semiconductors and Other Materials. *Prog. Quant. Elect.* **1993**, *17*, 299−338.
(118) Wang, J.; Blau, W. J. Inorganic and Hybrid Nanostructures for Optical Limiting. *J. Optics A- Pure and Appl. Optics* **2009**, *11*, 024001.
(119) Porzi, C.; Guina, M.; Bogoni, A.; Poti, L. All-Optical Nand/Nor Logic Gates Based on Semiconductor Saturable Absorber Etalons. *IEEE J. Sel. Top. Quant.* **2008**, *14*, 927−37.
(120) Castilla, S.; Terrés, B.; Autore, M.; Viti, L.; Li, J.; Nikitin, A. Y.; Vangelidis, Y.; Watanabe, K.; Taniguchi, T.; Lidorikis, E.; Vitiello, M. S.; Hillenbrand, R.; Tielrooij, K. J.; Koppens, F. H. L. Fast and Sensitive Terahertz Detection Using an Antenna-Integrated Graphene pn Junction. *Nano Lett.* **2019**, *19*, 2765−2773.
(121) Wang, H.; Strait, J. H.; George, P. A.; Shivaraman, S.; Shields, V. B.; Chandrashekhar, M.; Hwang, J.; Rana, F.; Spencer, F. M.; Ruiz-Vargas, C. S.; Park, J. Ultrafast Relaxation Dynamics of Hot Optical Phonons in Graphene. *Appl. Phys. Lett.* **2010**, *96*, 081917.
(122) Katsnelson, M. I. *Graphene: Carbon in Two Dimensions*; Cambridge University Press: Cambridge, 2012.
(123) Tinkham, M. Energy Gap Interpretation of Experiments on Infrared Transmission through Superconducting Films. *Phys. Rev.* **1956**, *104*, 845.

https://doi.org/10.1021/acsnano.1c04937
ACS Nano 2022, 16, 3613−3624